Modeling the 3D dynamic rupture of microearthquakes induced by fluid injection

Mosconi F.[1], Tinti E.[1,2], Casarotti E.[2], Gabriel A-A.[3], Rinaldi A.P.[4], Dal Zilio L.[5], and Cocco M.[2]

[1] La Sapienza Università di Roma, P.le Aldo Moro 5, 00185 Roma, Italia
[2] Istituto Nazionale di Geofisica e Vulcanologia, Rome, Italy
[3] Scripps Institution of Oceanography, UCSD, La Jolla, USA
[4] Swiss Seismological Service, Department of Earth Sciences, ETH Zürich, Switzerland
[5] Earth Observatory of Singapore, Nanyang Technological University, Singapore, Singapore,

Corresponding author: Francesco Mosconi (francesco.mosconi@uniroma1.it)

Key Points:

- 3D dynamic rupture simulations of microearthquakes on a pressurized fault, with pore pressure profiles determined from poroelastic models.
- Modest variations of dynamic stress drop determine the rupture mode, distinguishing self-arresting from run-away ruptures.
- Runaway ruptures can dissipate more energy than self-arresting ones which display cracks transition into pulses upon arrest.

Keywords: induced earthquake, self-arresting rupture, runaway rupture, pore pressure changes, dynamic rupture propagation.

Abstract

Understanding the dynamics of microearthquakes is a timely challenge with the potential to address current paradoxes in earthquake mechanics, and to better understand earthquake ruptures induced by fluid injection. We perform fully 3D dynamic rupture simulations caused by fluid injection on a target fault for FEAR experiments generating $M_w \leq 1$ earthquakes. We investigate the dynamics of rupture propagation with spatially variable stress drop caused by pore pressure changes and assuming different constitutive parameters. We show that the spontaneous arrest of propagating ruptures is possible by assuming a high fault strength parameter S, that is, a high ratio between strength excess and dynamic stress drop. In faults with high S values (low rupturing potential), even minor variations in D_c (from 0.45 to 0.6 mm) have a substantial effect on the rupture propagation and the ultimate earthquake size. Our results show that modest spatial variations of dynamic stress drop determine the rupture mode, distinguishing self-arresting from run-away ruptures. Our results suggest that several characteristics inferred for accelerating dynamic ruptures differ from those observed during rupture deceleration of a self-arresting earthquake. During deceleration, a decrease of peak slip velocity is associated with a nearly constant cohesive zone size. Moreover, the residual slip velocity value (asymptotic value for a crack-like rupture) decreases to nearly zero. This means that an initially crack-like rupture becomes a pulse-like rupture during spontaneous arrest. In summary, our findings highlight the complex dynamics of small earthquakes, which are partially contrasting with established crack-like models of earthquake rupture.

Plain language

Understanding small earthquakes, especially those induced by underground fluid injection, is crucial in earthquake science. In our study, we reproduce these events using computer simulations on a 50 meter wide fault, aiming to understand how fluid-induced stress changes affect the earthquake behavior. We find that earthquakes can stop under specific conditions, specifically when fault strength largely exceeds the difference between on-fault stress before and after the earthquake. Minor changes in rock properties, like static to dynamic friction transitions, significantly impact earthquake size. Our research also shows that stress variations on faults can determine if the earthquake is growing or arresting. We observe a significant spatial extension of the earthquake arrest phase, noting differences in features compared to earthquakes that exhibit accelerating rupture propagation. This distinct behavior is linked to the stress heterogeneity due to pore pressure gradient within the fault. Overall, our findings reveal the complex dynamics of small earthquakes, which is partially contrasting with the conventional crack theory.

1. Introduction

The study of earthquake mechanics and the analysis of source properties has been mainly focused on moderate to large seismic events (Kanamori, 2003; Schmedes et al., 2010; Harris, 2017; Abercrombie, 2021). The investigation of the rupture process in micro-earthquakes, with magnitudes ranging between -4 and 2, has so far been carried out by spectral analysis of recorded data to derive source parameters such as seismic moment, source radius, stress drop and corner frequency (Imanishi and Ellsworth, 2006; Allmann et al., 2007, 2009; Selvadurai, 2019; Abercrombie, 1995, 2021; Abercrombie and Rice, 2005; Cocco et al., 2016; 2023). These studies have been largely motivated by the need to constrain the scaling of earthquake source parameters – such as stress drop, radiated energy, source radius, and fracture energy – with seismic moment or total coseismic slip, laying the groundwork for our current understanding.

More recently, the emerging focus on induced seismicity and its related hazards has provided an opportunity to analyze faults more closely, improving our understanding of the dynamics that govern rupture initiation (Ellsworth, 2013; Grigoli et al., 2017; Moein et al., 2023; Galis et al., 2017). This was further promoted by the numerous laboratory experiments designed and performed to study the onset of dynamic instabilities in response to fluid injection on the rock sample, which provided relevant observations on induced laboratory earthquakes under controlled conditions (Scuderi and Collettini, 2016, Cappa et al., 2019; Hunfeld et al., 2021; Bolton et al., 2023; Volpe et al., 2023). While numerous studies on source complexity have concentrated on large earthquakes due to their associated severe damage and hazards, a persistent, unresolved, question in earthquake mechanics concerns the degree of heterogeneity and complexity influencing the rupture processes of microearthquakes. Furthermore, to the best of our knowledge, no studies have investigated the 3D rupture propagation and arrest of induced microearthquakes — an essential aspect in bridging the knowledge gap concerning induced seismicity and its relationship with microearthquakes.

Investigating the dynamics of microearthquakes necessitates the precise determination of constitutive parameters such as stress, friction, and critical slip at small spatial scales (millimeters to centimeters), which are crucial for understanding rupture propagation over meter-scale distances (1-100 m). Given the challenges in constraining source parameters using surface or near-surface data, innovative approaches have been proposed and adopted to collect near-source data and observations. These approaches include utilizing deep boreholes that intersect fault surfaces (Zoback et al., 2011; Tobin et al., 2022, among several others) as well as underground laboratories providing access to fault zones at depths ranging between a few hundreds and a kilometer (Guglielmi et al. 2015; Lesko; 2015; among many others). Within this array of monitoring systems (deep borehole, underground labs and deep mines), the Bedretto Underground Laboratory for Geosciences and Geoenergies (BULGG) in the Swiss Alps provides access to a volume of crystalline faulted rocks at depth of 1000-1500 m (Ma et al., 2022; Achtziger et al., 2024). BULGG hosts the FEAR (Fault Activation and Earthquake Ruptures) ERC-Synergy project (Meier et al.; 2024) that aims at reactivating a natural fault under controlled conditions by stimulating the nucleation of a target earthquake of magnitude $M_w = 1$. This event will be recorded with a dense multi-disciplinary on-fault monitoring system. Among several faults classified along the whole tunnel, the target fault for FEAR experiments, named hereinafter MC fault, has been identified (Achtziger et al., 2024; Volpe et al., 2023). The information required to constrain dynamic rupture simulations (e.g., Harris et al., 2018), including the fault geometry and stress state (slip tendency, stress orientation) as well as its frictional properties (Volpe et al., 2023) is available. Planned stimulation experiments within this fault zone, spanning 50-100 meters, will adhere to a precise injection protocol (Meier et al., 2024). The dedicated on-fault monitoring system is designed to capture microseismicity across a wide magnitude range (Mw -6 to 1), offering an unparalleled opportunity to examine the complex dynamics of rupture nucleation and propagation during microearthquakes within the magnitude range between 0 to 1.

The role of fluids in earthquake mechanics is well-documented in in natural tectonic settings, anthropogenic activities, and laboratory experiments (Rice, 1992; Cocco and Rice, 2002; Miller et al., 2004; Ellsworth, 2013; Guglielmi et al., 2015; Viesca and Garagash, 2015; Martinez Garzon et al., 2016; De Barros et al., 2018; Cappa et al., 2019; Wang et al., 2024, and reference therein). Fault reactivation can result from an increase in the pore pressure P_f (Hubbert and Rubey, 1959; Scholz, 1990), leading to a reduction in the effective normal stress ($\sigma_n^{'} = \sigma_n - P_f$) thereby influencing the frictional strength of the fault. In recent years, the growing energy demand, both fossil and renewable, has led to an increase in the activities related to the underground fluid injection. This requires to pose more attention on the hazard of the induced and triggered seismicity, in the context of oil and gas reservoir, underground carbon dioxide sequestration and geothermal energy (Ellsworth, 2013; Candela et al., 2018, Moein et al., 2023). Some examples of notable earthquakes associated to fluid injection are the 2011 M_w 5.7 and 5.0 earthquakes near Prague in Oklahoma, United States (Keranen et al., 2013), the M_w 5.8 Pawnee, Oklahoma, in 2016 (Yeck et al., 2017) and the 2017 M_w 5.5

earthquake near an enhanced geothermal site in Pohang, South Korea (Grigoli et al., 2018; Kim et al., 2018; Lee et al., 2019, Palgunadi et al., 2020).

Numerous studies analyzed fault slip reactivation under elevated pore pressure, and both fluid-driven seismic and aseismic slip has been observed within a complex spectrum of fault-slip behavior (Garagash and Germanovich, 2012; Cappa et al., 2019; Larochelle et al., 2021; Dal Zilio et al., 2022; Ciardo and Rinaldi, 2022; Bolton et al., 2023). Experimental studies across various scales have highlighted the emergence of a zone characterized by aseismic slip, or creeping, adjacent to the injection point (Cornet, 2012, 2016; Garagash and Germanovich, 2012; Guglielmi et al., 2015; Scuderi and Collettini, 2016). The nature of the stress state in the stimulated fault zone influences this aseismic slip, leading to strain-energy accumulation outside the slipping area. This process continues until a critical nucleation length is reached, at which point a dynamic instability can propagate (Uenishi and Rice, 2003; Cebry et al., 2022).

Upon nucleation, the rupture propagates dynamically, characterized by high slip velocities and rupture speeds, generating seismic waves. The arrest of the rupture occurs when the rupture front does not possess enough energy to continue propagating. While the mechanisms of natural earthquake arrest are still debated (Kame and Yamashita, 1999; Galis et al., 2019; Ke et al., 2022; among several others), dynamic rupture models typically assume locally low-stress or high frictional strength, for example by prescribing spatial heterogeneities of the shear stress or static friction coefficient (Das & Aki, 1977; Harris et al., 2018; Ramos et al., 2021).

The study of rupture propagation and arrest in induced earthquakes allows the differentiation between self-arrested and runaway ruptures. The former refers to ruptures that spontaneously stop at a finite distance from the nucleation zone often remaining within the pressurized patch, while the latter describes ruptures that extend across the entire fault, ceasing only at fault boundaries due to geometrical complexities, stress or strength heterogeneities (Galis et al., 2017; Ke et al., 2018, 2022). This classification elucidates the rupture dynamics without necessarily invoking heterogeneous stress patches. Galis et al., (2017) pointed out that, while injection-induced earthquakes may cause severe seismic hazard, they also represent an opportunity to gain insights in earthquake physics. They used a linear slip weakening law to model an induced rupture and Linear Elastic Fracture Mechanics (LEFM) to interpret the transition between self-arresting and runaway induced earthquakes. They found that this transition is mainly controlled by frictional parameters and stress heterogeneity. Additionally, these authors corroborate the dependence of the expected magnitude of the induced earthquake on the radius of the pressurized area and on the injected fluid volume (Mc Garr, 2014; Galis et al., 2017; De Barros et al., 2019; Moein et al., 2023). However, a fundamental physical explanation of why dynamic rupture arrests or can continue propagating is still elusive.

In this study, we concentrate on the spontaneous dynamic simulation of rupture processes for induced earthquakes with a maximum magnitude of less than 1 (Mw < 1). Our simulations encompass the full dynamics of earthquake rupture and seismic wave propagation within a 3D volume, based on a linear slip-weakening model to describe shear stress evolution at the rupture front and initiated by pore fluid pressurization. We apply our model to the target fault within the Bedretto Underground Laboratory for Geosciences and Geo-energies (BULGG) at an approximate depth of 1500 meters.

The aim of this study is to simulate the propagation and the arrest of dynamic ruptures on the pressurized fault selected for FEAR experiments. The fault is characterized by initially uniform frictional parameters and is subjected to uniform prestress. This simplified initial stress condition is adopted to emphasize the role of pore pressure changes on spontaneous dynamic rupture propagation. A realistic pore pressure profile caused by fluid injection in a nucleation patch is simulated considering the poroelastic response of the fault zone. The rupture process during induced microearthquakes is investigated to shed light on the key features of dynamic propagation as well as the constitutive parameters influencing the extent of the rupture before its arrest, determining the magnitude of the induced earthquake.

2. Methods and Source Parameterization

We utilize the open-source software SeisSol (www.seissol.org) to model the 3D spontaneous rupture propagation of micro-earthquakes on a 3D fault plane. SeisSol is based on the arbitrary high-order derivative discontinuous Galerkin (ADER-DG) method (Dumbser and Käser, 2006), and solves the 3D elastodynamic equation for spontaneous frictional failure on a prescribed fault surface, whereas for the seismic wave propagation it computes the elastic wave equation in heterogeneous media (Pelties et al., 2012). The applicability of SeisSol has been verified in various earthquake scenarios, ranging from models including a simple planar fault to more complex fault geometries involving geometric discontinuities, non-planarity, fault roughness, and multiple intersecting adjacent fault branches (Harris et al., 2018; Ulrich et al., 2019; Tinti et al., 2021; Taufiqurrahman et al., 2022; Biemiller et al., 2023, Gabriel et al., 2023). This study presents the first dynamic rupture simulation for an induced micro-earthquake on a decametric-scale planar fault (50 m length), under stress conditions determined by fluid injection and pore-pressure changes.

2.1. Linear slip-weakening friction law

Dynamic earthquake modeling requires the use of a fault constitutive law which describes shear traction evolution in each point on the fault characterizing the breakdown stage and dynamic weakening near the rupture front. Different constitutive laws analytically describe the shear stress as a function of diverse constitutive variables, such as slip, slip velocity, state, and temperature. Here, we adopt the linear slip-weakening (LSW) constitutive law (Ida, 1972) because it is simple and allows the clear definition of fracture energy and a direct control on different key parameters such as fault strength and dynamic stress drop during the rupture propagation.

This constitutive relation is characterized by the peak stress value on the fault $\tau_p = \mu_s\, \sigma'_n$, the dynamic residual (i.e., frictional) stress level $\tau_d = \mu_d\, \sigma'_n$, and the critical slip distance D_c, as

$$\tau = \begin{cases} \left[\mu_s - (\mu_s - \mu_d)\frac{\delta}{D_c}\right]\sigma'_n\,, & \delta < D_c \\ \mu_d \sigma'_n\,, & \delta > D_c \end{cases} \tag{1}$$

where μ_s and μ_d are the static and dynamic friction coefficients, respectively, σ'_n is the effective normal stress and δ the slip. When the shear stress reaches its peak value the fault starts slipping and the shear stress decreases linearly from the peak to the residual stress value over a critical slip distance D_c. This breakdown stress drop ($\Delta\tau_p = \tau_p - \tau_d$) corresponds to a friction decrease from the static to the dynamic friction coefficient. Once the slip exceeds the critical slip distance (D_c), the shear traction becomes independent of slip and equal to the residual dynamic stress level $\tau_d = \mu_d\, \sigma'_n$. The final stress is equal to the residual stress level, and stress overshoot or undershoot are not considered. The energy dissipated to sustain the rupture propagation, namely the fracture energy, depends on the values of the breakdown stress drop and the critical slip weakening distance D_c.

According to equation (1), the strength excess ($\tau_p - \tau_0$) is defined as the difference in shear stress between its peak and initial values, with the peak stress being equal to the yield strength of the fault. The strength excess occurs with no slip and is associated with a linear elastic and reversible process. The dynamic stress drop ($\Delta\tau_d = \tau_0 - \tau_d$), is the stress released during the dynamic weakening. Because the final stress is equal to the residual dynamic stress level (τ_d), the dynamic and static stress drop are the same. The ratio between the stress excess and the dynamic stress drop is the strength parameter S, as defined by the pioneering paper of Andrews (1976):

$$S = \frac{(\tau_p - \tau_0)}{(\tau_0 - \tau_r)} \tag{2}$$

Previous studies dealing with modeling earthquake ruptures have emphasized the importance of computing the non-dimensional strength parameter S that allows us to describe the potential of the fault to develop a rupture (Andrews, 1976; Das & Aki, 1977; Geubelle & Kubair, 2001; Liu & Lapusta, 2008; Barras et al., 2023). Andrews (1976) found that the parameter S controls the transition of a crack from sub-shear rupture to supershear rupture propagation. More recent studies have also demonstrated its significance in influencing rupture style (Gabriel et al., 2012; Bai and Ampuero, 2017) or its role in the context of induced seismicity (Galis et al., 2017). The parameter S measures the material strength (strength excess) relative to the stress release during dynamic rupture (dynamic stress drop). The strength excess quantifies the necessary stress to be concentrated at the rupture front, from the initial to the peak shear stress, needed for the propagation. On the other hand, the dynamic stress drop encompasses the stress released during the dynamic breakdown referred to the initial shear stress, characterizing the tectonic loading of the fault before the initiation of a dynamic rupture.

The LSW constitutive law allows the interpretation of key features of the dynamic rupture propagation in terms of a few parameters, even in a very sensitive condition such as an induced earthquake. The advantage of working in a well constrained in-situ boundary condition, as provided by the Bedretto Lab, helps to decrease the a-priori assumptions and to investigate the dynamics of microearthquakes focusing on the less poorly constrained constitutive parameters (such as the critical slip distance D_c).

2.2. Fault model and input parameters

We simulate a dynamic rupture scenario, for an induced earthquake, on a 60° dipping normal fault, embedded in a 3D elastic medium, with a P-wave speed of 2621 m/s, S-wave speed of 1531 m/s and a density of 2620 kg/m^3. To accurately define the fault geometry, we leverage in-situ geological and geophysical characterizations of the target fault, conducted as part of the FEAR project in the Bedretto Tunnel. These characterizations, detailed in Achtziger et al. (2024), reveal that the target fault exhibits an approximately planar geometry, extending laterally for about 250 meters. In our model we consider a volume of 200 x 200 x 200 m and a fault dimension of 50 x 50 m, representing the fluid pressurized portion of the larger MC fault zone (Figure 1a). The computational domain is discretized using an unstructured mesh, with a total number of ~69 million tetrahedral elements. The elements in the volume change in size, transitioning from 12 cm length close to the fault to a maximum value of 15 m at the volume edge, in order to maintain both computational efficiency and high resolution, simultaneously. The well-constrained in-situ boundary conditions of the Bedretto Tunnel allow us to include a realistic on-fault stress state with negligible spatial variations due to the small fault dimension here considered. Therefore, we impose a constant normal and shear stress on the fault prior to fluid injection, with the former prescribed at $\sigma_n = 22.7$ MPa and the latter to $\tau_0 = 4.7$ MPa. The static (μ_s) and dynamic (μ_d) friction coefficients are considered homogeneous and constant over the fault. The static friction is $\mu_s = 0.58$, while the dynamic friction is assumed to be $\mu_d = 0.21$ for the first set of Models A and $\mu_d = 0.15$ for the second set of Models B that will be discussed in the paper. The initial resulting stress conditions after the stress perturbation due the injection of fluid within each specific set of models will be described more in detail in the subsequent Section 3.

A crucial parameter in dynamic rupture simulations is the on-fault resolution to capture the stress dissipation in the cohesive zone, i.e. the spatial dimension along fault where the shear stress weakening occurs, evolving from the peak value to the residual level. Based on the extended analysis conducted by Wollherr et al. (2018) to achieve a well resolved cohesive zone we adopt a spatial discretization with an on fault mesh element size of 12 cm with a mean cohesive zone dimension of 0.34m (detailes in Supplementary material)

3. Stress changes from fluid injection

The main goal of this work is to investigate the characteristics of a dynamic rupture resulting from on-fault fluid pressurization, exploring various scenarios to understand the conditions leading to a self-arresting rupture with $M_w < 1$, as opposed to a runaway earthquake that ruptures the entire fault surface, resulting in a $M_w > 1$.

3.1. Pore pressure changes profile

In order to create realistic pressure conditions on the fault zone, we employ the software TOUGH3-FLAC3D, that allows the simulation of coupled fluid flow and geomechanics

(Rinaldi et al., 2022). This approach aims at simulating complex non-linear behavior potentially occurring in the vicinity of the injection point, as well effects of a packed interval. The coupled approach allows us to account for full poroelasticity via porosity evolution as well as variation of permeability as function of geomechanical parameters (e.g. stress or strain). We develop a first-order model (50 m X 50 m X 50 m) with a fault zone dipping 60˚, 20 cm thick, and cutting through an homogenous medium.

Initial conditions follow the state of stress found at the BedrettoLab (Bröker & Ma, 2022, Bröker et al., 2023), with minimum horizontal stress at 20 MPa, maximum horizontal stress at 25 MPa, and vertical stress at 31 MPa for the injection region. The initial pore pressure at the injection is set at 3.8 MPa. We impose constant stress and pressure at all boundaries. In terms of rock properties, the fault zone is assumed weaker than the surrounding formation, with a Young's modulus of 5 GPa compared to 15 GPa of the host rock. The Poisson's ratio is set to 0.25 in the entire domain. We neglect poroelastic effects by assuming a near-zero Biot's coefficient (0.001).

The permeability of the fault zone is assumed constant at 10^{-15} m^2, representing a fractured region within homogeneous granite with permeability set at 10^{-18} m^2. The injection region at the center of the model is set as a 1 m^2 patch, with permeability changing as a function of the normal effective stress (Rinaldi & Rutqvist, 2019). Porosity is set to 1% in the entire domain.

We simulate 24 hours of injection at constant flow rate (0.012 kg/s), simulating a constant pressure of about 14.5 MPa at the injection point, and allowing fluids to propagate along the fault. The given pressure is the one observed to be the jacking pressure in several injections at the BedrettoLab (Bröker et al., 2023). In TOUGH-FLAC, the given conditions would reactivate the fault within the next numerical time step with a further increase in pressure when assuming a fault zone with a friction angle of 31˚, yielding a static friction coefficient of 0.6 very similar to the value adopted for dynamic simulations (0.58). Hence, we stop our simulation at the time step before earthquake nucleation on the fault would occur. The simulated pressure profile (Figure 1b) is then used as the starting point for the dynamic rupture model and it is considered representative of key physical conditions during direct injection into a fault zone.

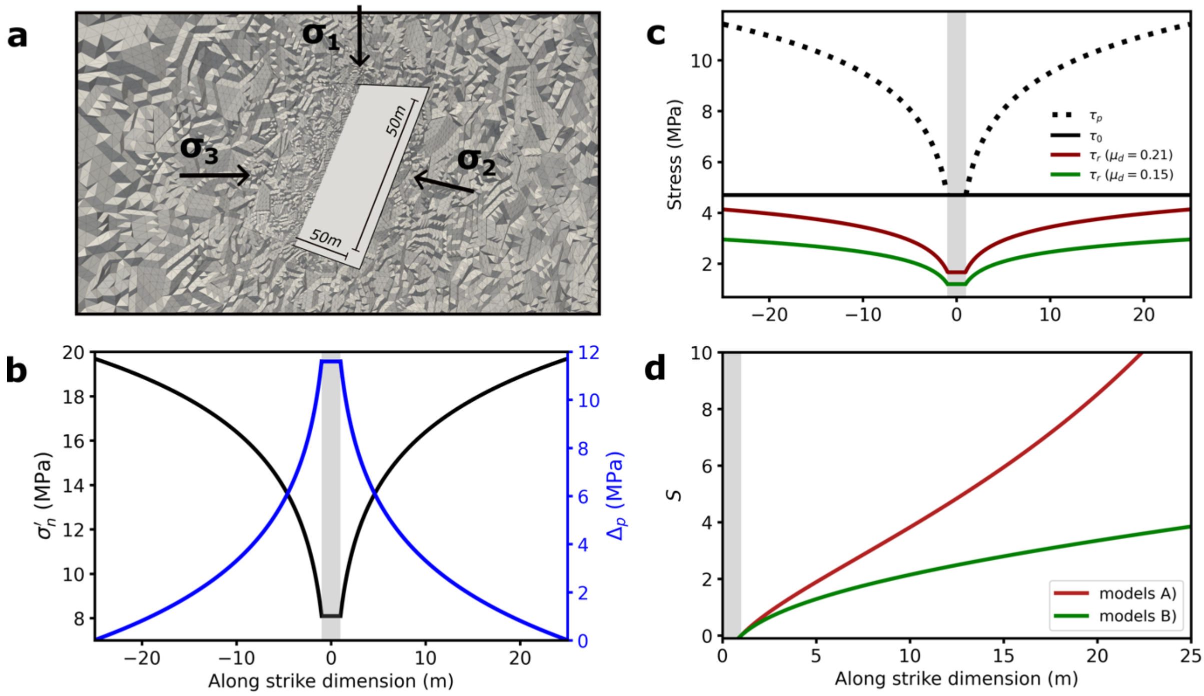

Figure 1. 3D dynamic rupture model setup. **(a)** Adopted fault geometry and grid size (50 x 50m), volumetric computational mesh (200 x 200 x 200m) and principal stress orientations. **(b)** Profile of pore-pressure change of the 25m radius pressurized fault patch (blue line) and on-plane effective normal stress (black line). The gray bar shows the position of the injection borehole. **(c)** Spatial profile of the resulting stress parameters after the fluid pressurization. The peak stress (or static fault strength, black dashed line) and the initial shear stress (black solid line) are the same for both the class of Models A and B, which differ for the residual stress level because of the different adopted dynamic friction coefficients (red solid line 0.21 and green solid line 0.15). **(d)** Evolution of the strength parameter S (Eq. 2) for half-fault dimension for the set of Models A and B (red line and green line, respectively).

3.2. Modeled stress conditions

Figure 1-b shows the pore pressure and normal stress profiles resulting from fluid injection into the modeled fault patch: the effective normal stress is minimal in the injection zone (gray shaded bar) and increases along the strike direction as pore pressure decreases.

Figure 1c illustrates the spatial distribution of the on-fault stress parameters. The peak stress or the fault static strength ($\tau_p = \mu_s\, \sigma'_n$) is shown by a black dashed line and it increases from the fault center (injection point) towards the fault boundary due to the increase of σ'_n (Figure 1b). The initial stress (solid black line) is constant over the whole pressurized fault patch. At the center of the fault, the peak stress is equal to the initial shear stress meaning that the strength parameter is zero and the rupture can nucleate. The fault portion affected by the nucleation is represented with the gray bar. The residual shear stress also increases within the fault radius because of the effective normal stress gradient. It is important to note that all the discussed stress conditions are valid across the different fault directions, implying a radial parametrization.

As anticipated above, we simulate here two sets of models distinguished for the value of the assumed dynamic friction coefficient: Models A (solid red) dynamic friction is $\mu_d = 0.21$, while in Models B $\mu_d = 0.15$. Although peak stress remains similar between Models A and B, variations in dynamic friction lead to differences in breakdown and dynamic stress drop values, as well as spatial stress gradients along the fault. The spatial gradient of the effective normal stress (σ'_n) also determines the spatial variability of the parameter S (Figure 1d), which is due to the spatial increment of the strength excess coupled with the reduction in the dynamic stress drop along the fault radius. This implies a quite different spatial gradient of the strength parameter S for the two sets of Models (A and B), as shown in Figure 1d for half fault dimension.

As we will discuss in the following, each set of models yields different behaviors of dynamic rupture propagation for different ranges of the critical slip weakening distance: namely, Models A yield self-arresting ruptures and Models B runaway ruptures. This confirms that the S parameter plays a crucial role in the behavior of dynamic rupture propagation for induced earthquakes. It is worth observing that in our simulation, we intentionally did not include any additional heterogeneity of the initial stress or other constitutive parameters, because we are going to focus on the role of pore pressure and effective normal stress (σ'_n) changes caused by the fluid injection. In the following we will examine the influence of the S parameter on the behavior of dynamic rupture propagation and arrest in the context of induced seismicity.

3.3. Rupture nucleation

The earthquake nucleation zone is located at the fault injection point by assuming that the fault strength (initial stress value) equals the peak shear stress, the latter being determined by the pore-pressure peak caused by fluid injection (see Figure 1). In models of single dynamic rupture events, we generally adopt the assumption of artificial rupture initiation to enable more computationally efficient simulations. (Dalguer & Day, 2009; Bizzarri, 2010; Galis et al., 2015). Indeed, accounting for spontaneous nucleation due to an increasing tectonic loading in time (Uenishi and Rice, 2003, Rubin and Ampuero, 2005) requires different model parametrization, a friction law that accounts for the fault strength recovery (i.e., Rate & State friction law) and different numerical algorithms, e.g., an adaptive time stepping scheme during the simulation of the full seismic cycle (Lapusta and Liu, 2009) solvers suited for elliptic instead of hyperbolic partial differential equations (Uphoff et al., 2023), which are adopted for simulations of sequences of earthquakes and aseismic slip (e.g., Barbot et al. 2012; Jiang et al., 2022).

In general, a dynamic rupture necessitates to first reach a critical length before spontaneously growing, leading to an unstable propagation. A relation to estimate the universal critical nucleation length for homogenous condition of the in-plane crack under slip weakening friction law has been provided by Uenishi & Rice (2003):

$$l_c = 1.158 \frac{1}{(1-\nu)} \frac{G\, D_c}{\Delta\tau_b} \tag{3}$$

where, G is the shear modulus, ν the Poisson's ratio, D_c the critical slip weakening distance and $\Delta\tau_b$ is the breakdown stress drop.

There are two nucleation approaches mainly adopted in the literature for dynamic rupture simulations: initiation through a time-weakening law where the rupture front velocity is imposed (Andrews, 1985) or the overstressed patch leading to instantaneous nucleation patch failure (Kanamori, 1981). This study adopts a slightly modified rupture initiation method, tailored to the unique stress conditions induced by fluid stimulation and the subsequent reduction in effective normal stress. We assume a constant time-independent pore pressure value within the injection zone corresponding to a borehole radius of 1 m and representing the maximum pressure change (Figure 1b, Section 3.1). This fluid pressure plateau represents the initial region where the fault strength equals the initial shear stress level, and consequently the rupture is able to nucleate. To achieve a gradual and smooth increase in fault slip rate at the hypocenter from ~10^$^{-2}$ m/s to typical seismic slip velocity values for dynamic rupture simulations (~10^0 m/s), we impose a slightly smaller D_c = 0.4 mm within the nucleation patch for all models. A quantitative formulation which would allow us to estimate the critical size of the nucleation patch in 3D and under non-homogeneous normal stress conditions is elusive. We therefore use equation (3) to develop an estimate of the size of the nucleation patch. Equation 3 predicts a critical nucleation half-length varying between 0.7 and 1.2m due the variation in breakdown stress drop and the different adopted D_c values. In agreement with this estimate, in our simulations the nucleation patch size is adopted from the poro-elastic simulations protocol of fluid injection (1 m bore hole size), with a nucleation behavior consistent across all models. The adopted stress and constitutive conditions allow us to maintain the same nucleation patch size in all our simulations because the fault strength reduction along the source radius is determined by the imposed pore-pressure profile resulting from poro-elastic modeling.

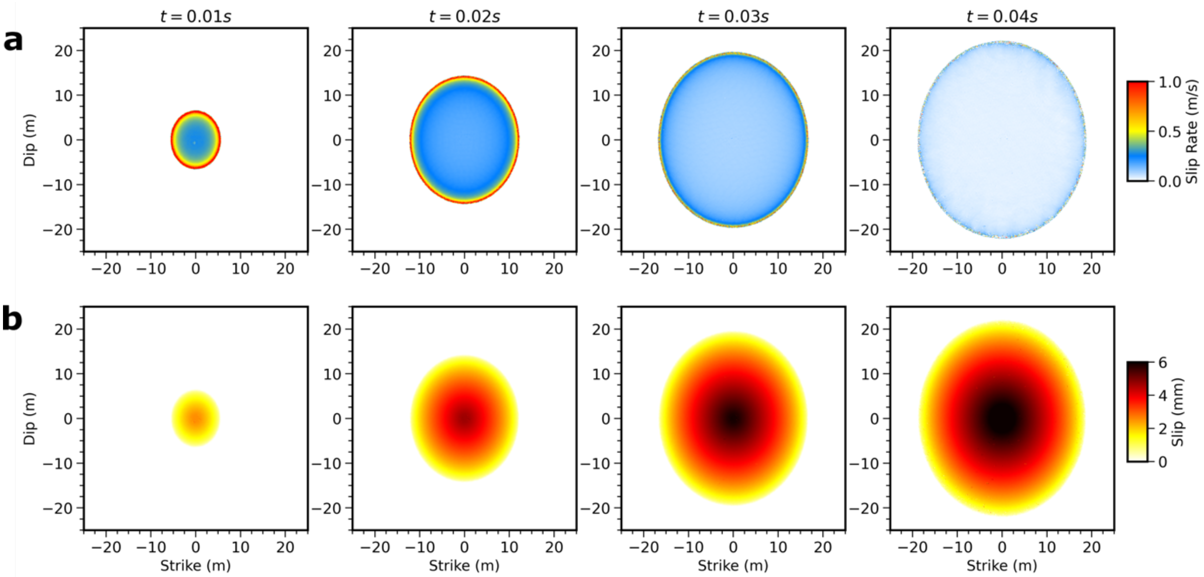

Figure 2. Evolution of the dynamic rupture for the model with D_c = 0.6 mm belonging to the class of Models A. **(a)** Snapshots of the slip rate during the rupture propagation. **(b)** Snapshots of the accrued cumulative slip. Color scales display values of slip rate and slip.

4. Results

We present a series of 3D simulations of the spontaneous propagation of dynamic rupture along a pressurized fault with a spatial pore pressure profile constrained by poroelastic simulations aimed at reproducing a stimulation experiment envisioned in the FEAR project. As described above, the fault geometry and parameterization are taken from the target fault zone of the FEAR project in the Bedretto underground laboratory (BULGG). We investigate two classes of Models characterized by different values of the dynamic friction coefficient: Models A have dynamic friction μ_d equal to 0.21, while in Models B μ_d is 0.15. For each class of Models we use different ranges of the critical slip weakening distance. In the following we present the results of our simulations for each class of Models.

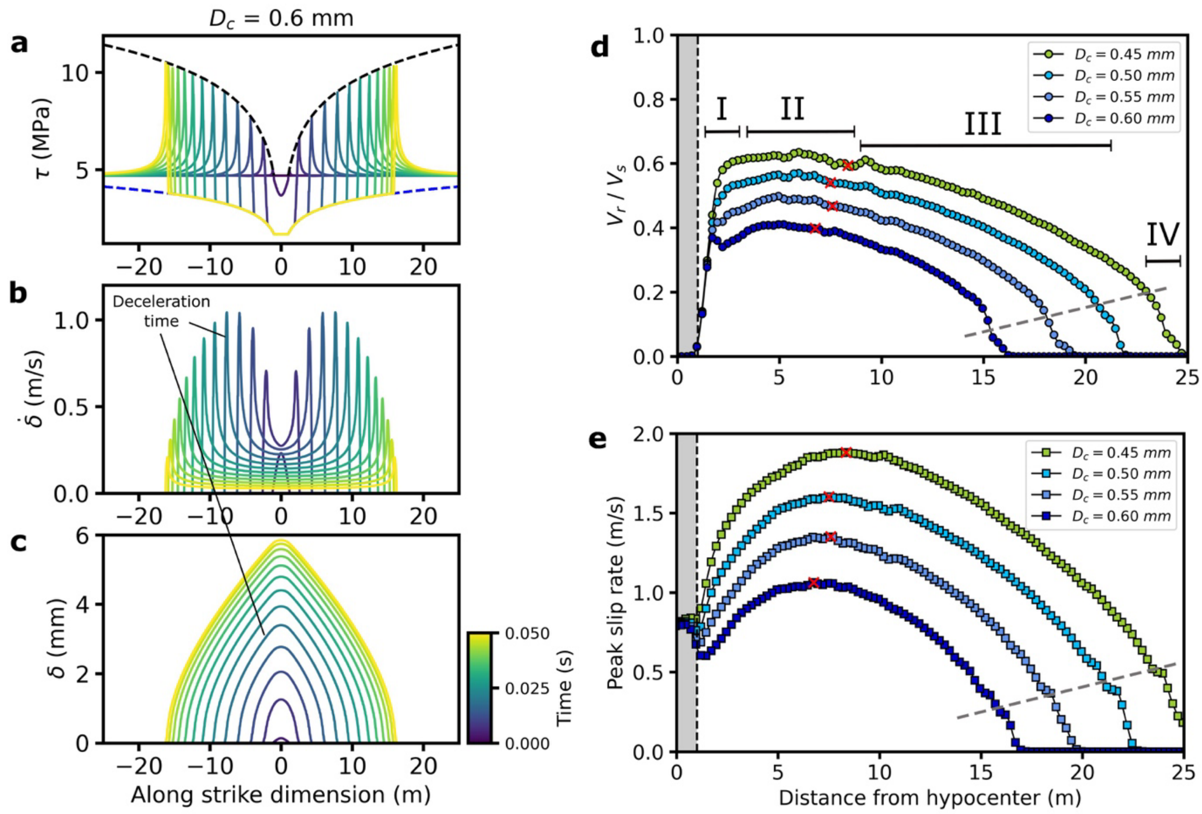

Figure 3. Illustration of the set Models A with imposed $\mu_d = 0.21$ for an along-strike section. **(a-c)** Example of rupture evolution through different snapshots of shear stress (τ), slip velocity ($\dot{\delta}$) and slip profile (δ), the colormap indicates the temporal evolution of the rupture. **(d)** Rupture speed and peak slip rate **(e)** as a function of the hypocentral distance (injection point). The four stages shown in panel d have been drawn for the model with $D_c = 0.45$ mm. Red stars mark the end of phase II, corresponding to the respective maximum in peak slip rate for each model. Color scale displays temporal evolution in panels a-b-c and adopted D_c values in panels d, e.

4.1. Self-arresting earthquakes

We first analyze the set of Models A ($\mu_d = 0.21$) and explore a range of D_c values ranging from 0.45 mm to 0.6 mm. The dynamic models computed with these parameters are characterized by self-arresting ruptures, which results in induced earthquakes with $M_w < 1$. Figure 2 shows the evolution of a propagating rupture for a model with $D_c = 0.6$ mm: Panel (a) displays the snapshots of slip velocity at different times, while Panel (b) shows the snapshots of cumulative slip. The slip distribution shown in Panel b resembles those observed in natural earthquakes and laboratory experiments. (Scholz & Lawer, 2004; Ke et al., 2018). Given the source parameterization, the rupture propagates with nearly radial symmetry. This symmetry provides

a basis for detailed examination of shear stress, slip velocity, and slip evolution along specific orientations, including the along-strike direction – a focal point of our subsequent analysis.
Figure 3 shows the shear stress, slip velocity and slip evolution with respect to the fault strike direction during dynamic rupture propagation computed for D_c = 0.6 mm (panels a, b and c, respectively), which displays the key features of self-arresting ruptures over a source radius of nearly 15 m. The evolution of shear stress, slip velocity and slip in the along-dip direction is detailed in the Supplementary Material (Figure S1a, b, c). Comparing Figures 3a-c and S1a-c confirms that, despite minor differences in rupture velocities, the along-dip results are similar to those retrieved analyzing propagation along-strike direction. The initial increase of peak slip velocity is followed by a gradual decrease during the arrest stage resulting in the retrieved spatial slip gradient. This slip rate behavior implies a crack-like rupture (Kostrov, 1964), meaning that all points behind the rupture front continue to slip until the rupture arrest. Peak and residual stress values change with position along the strike because of the variable effective normal stress (Figure 1).
The breakdown stress drop increases during rupture propagation, because the increase of peak shear stress along the fault radius is larger than the increase of residual stress. Panels d and e of Figure 3 summarize the behavior of dynamic ruptures for the four simulations conducted with D_c ranging from 0.45 mm to 0.6 mm showing the rupture velocity and peak slip rate, respectively, with respect to half-strike dimension. The vertical gray-shaded bar indicates the size of the nucleation patch adopted in all simulations, while the red stars identify the points along the fault where each rupture model reaches its maximum peak slip velocity, (Figure 3 e). The behavior of rupture velocity and peak slip rate allows us to subdivide the rupture propagation in four distinct stages (Figure 3d). The first stage (I) corresponds to the initial rapid acceleration of the rupture front outside the nucleation patch associated with rapidly increasing peak slip rate. This stage is followed by a propagation at nearly constant rupture velocity characterized by smoothly increasing peak slip rate reaching its maximum value during propagation (stage II). At this point, the dynamic rupture starts to decelerate. We have distinguished two stages during rupture deceleration: stage III is characterized by a continuous decrease of rupture velocity with a progressive decrease of peak slip rate, followed by stage IV in which rupture velocity and peak slip velocity abruptly drop to zero. The inferred four stages describe acceleration, propagation, deceleration, and arrest of dynamic rupture propagation, as clearly pointed out by the spatial evolution of rupture speed and slip rate.
Rupture velocity reaches its maximum value during the initial rupture acceleration (I) in a relatively small spatial extension; this maximum rupture speed is maintained during the

subsequent stage (II) preceding rupture deceleration (in stage III). The spatial extension of dynamic rupture during these first two stages slightly depends on the adopted D_c values, while on the contrary the rupture velocity values depend on the assumed values of the critical slip weakening distance D_c: the smaller D_c, the higher the rupture velocity values characterizing each simulation. During the acceleration stages (I and II), peak slip velocity continuously increases up to its maximum value marking the beginning of rupture deceleration. Inferred peak slip velocity values are inversely proportional to the critical slip weakening distance D_c (Figure 3 e).

Differently from the initial stages (I and II) characterized by rupture acceleration or propagation at nearly constant speed, the spatial extension of the deceleration stage (III) depends on D_c: the larger D_c, the smaller is the rupture area characterized by rupture deceleration. This implies that D_c together with the dynamic friction value control the dimensions of the final ruptured area and therefore the magnitude of the induced earthquake for self-arresting ruptures. It is interesting to observe that the rate at which the rupture decelerates appears to be similar among all models. Finally, all simulations display the arrest phase IV characterized by an abrupt decrease in both rupture speed and peak slip rate, as indicated by the gray dashed line in Fig. 3d-e. We note that all ruptures stop within the pressurized fault patch, with source radii ranging from approximately ~15 to ~24 m. The released moment magnitudes (M_w) are 0.76, 0.88, 0.97 and 1, respectively, increasing with decreasing D_c.

A self-arresting rupture generates a nearly triangular shape of the slip spatial profile (Figure 3 c), with a maximum slip of 5.8mm for the adopted D_c value (0.6 mm). During the initial rupture acceleration stages (I and II) slip reaches a peak value of ~3mm (at the injection point), as indicated by lines in Panel b-c highlighting the timestep when deceleration starts (the rupture front at this point is 6-7 m away from nucleation). This implies that only half of peak slip and less than half of the rupture extension has been reached during the acceleration of the rupture (phase I and II), determining a large portion of the seismic moment release during the deceleration stage (phase III and IV) (see Supplementary Material, Figure S3).

4.2. Runaway earthquakes

It is often assumed (Shapiro et al., 2011; McGarr, 2014) that a rupture remains confined within the volume affected by the pore pressure change, that is within the pressurized fault patch. However, if the dynamic load at the crack-tip is sufficiently large to sustain rupture propagation, the rupture can extend beyond the pressurized patch. This extension enables the rupture to encompass a larger fault area, consequently leading to an earthquake of greater magnitude. This is the case of the runaway ruptures investigated in this study. As anticipated above, the class of Models B relies on the assumption of a lower dynamic friction coefficient (namely, μ_d = 0.15) over the target fault, leading to runaway ruptures propagating outside the pressurized fault. For this class of Models B, we explored a range of D_c values ranging from 0.60 mm to 0.90 mm.

Figure 4 shows the shear stress, slip velocity and slip evolution along the strike direction (Panels a, b, c, respectively) for a simulation performed with D_c=0.6 mm, the same D_c value used in Figure 3 for self-arresting ruptures (the respective along-dip evolution is shown in Figure S2). The shear traction evolution displayed in Figure 4a shows the differing increase of peak and residual stress values with space, resulting in the increase of breakdown stress drop during the rupture propagation. The spatial increase of the strength parameter S (Figure 1d) is modest because the increase of strength excess (the same as model A) is counterbalanced by the larger dynamic stress drop (see equation 2). The peak slip rate continuously increases during propagation, maintaining a constant residual slip velocity value behind the rupture front coherently with crack-like ruptures. The maximum peak slip velocity is 6 m/s for this simulation with D_c=0.6 mm. The slip profiles (elliptical) shown in Panel e are also coherent with an accelerating crack-like rupture (Gabriel et al., 2012).

Figure 4-d and 4-e illustrates how rupture speed and peak slip velocity vary with respect to half fault strike dimension across different values of the critical slip weakening distance (D_c). After the initial rapid acceleration, the rupture front decelerates with smoothly increasing rupture velocity remaining within the sub-shear regime. Decreasing the adopted D_c value results in a faster acceleration and higher rupture velocities. This is why we explore slightly larger Dc values in Models B compared to those adopted in Models A, which would otherwise yield supershear rupture. Peak slip velocity continuously increases during propagation for all the adopted D_c values, with the largest peak slip rate values for the smallest D_c. The rupture propagates along the whole pressurized patch with an increasing peak slip velocity and without any deceleration. This characterizes the runaway ruptures. Our simulations suggest that, regardless of the adopted D_c value, obtaining a self-arresting rupture is not possible if the dynamic friction is imposed to 0.15, even when the chosen D_c value is approximately twice than that used in the class of Models A. For the set of parameters adopted in Models B, when rupture nucleates, it always propagates as a runaway rupture front. Rupture arrest for runaway ruptures occurs only if the rupture encounters a geometrical barrier or an area with unfavorable stress conditions outside the pressurized patch.

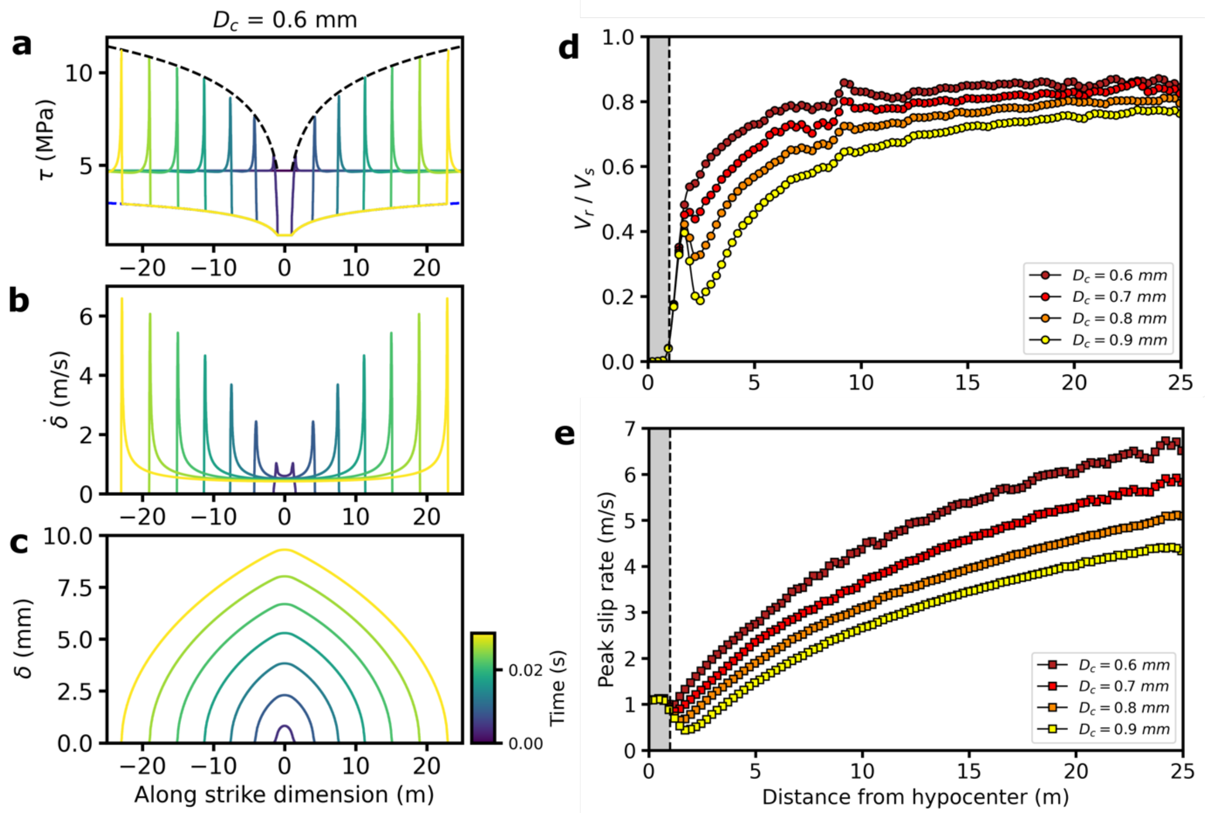

Figure 4. Illustration of the set Models B with imposed $\mu_d = 0.15$ for along-strike section. **(a-c)** Example of rupture evolution through different snapshots of shear stress (τ), slip velocity ($\dot{\delta}$) and slip profile (δ). **(d)** Rupture speed and peak slip rate **(e)** as a function of the hypocentral distance (injection point). Color scale displays temporal evolution in panels a-b-c and D_c values in panels d, e.

5. Discussion

In this study we have simulated self-arresting and runaway ruptures by stimulating a pressurized patch through fluid injection within the nucleating zone. Fluid injection maintains a constant peak of pore-pressure within the nucleation patch (1 m radius), where peak shear stress τ_p is imposed to be equal to the initial stress value. Fluid injection generates a spatial pore-pressure gradient decreasing towards the edges of the pressurized patch. Since the initial stress is deliberately maintained as homogeneous across the fault, the resulting spatial gradient of effective normal stress (Figure 1) causes spatially variable strength excess, breakdown and dynamic stress drops. Therefore, it is crucial to discuss the factors determining whether a rupture is self-arresting or runaway, characteristics that directly impact the moment magnitude of the induced earthquake and the associated seismic hazard.

5.1 Fracture energy

Models A and B differ in their dynamic friction coefficients and the range of employed critical slip weakening distances (D_c). It is important to point out that for Models B, which are characterized by a lower dynamic friction coefficient, all simulated dynamic ruptures are runaway ruptures for any adopted value of D_c. On the contrary, for simulations belonging to Models A, the self-arresting feature disappears if we decrease D_c below 0.2 mm. To understand this different behavior, we analyze for each model the fracture energy G_c, a crucial parameter to understand earthquake propagation and arrest (Andrews, 1976; Cocco et al., 2023; Gabriel et al. 2024, Arxiv).

For a linear slip-weakening constitutive law, G_c depends linearly on breakdown stress drop and D_c (Ida, 1972). Figure 5 shows the spatial evolution of fracture energy for self-arresting (panel a) and runaway (panel b) ruptures. Runaway ruptures dissipate more energy density (or breakdown work, Tinti et al., 2005) than self-arresting ruptures. Comparing the simulations performed with the same D_c value (0.6 mm) for the two classes of models, the self-arresting rupture (Models A) dissipates less fracture energy at the rupture front than the runaway rupture (Models B). This is because breakdown stress drop is larger for runaway ruptures belonging to the class of Models B (Figure 1b). Therefore, we conclude that self-arresting ruptures are not caused by a larger energy dissipation at the rupture front (i.e., fracture energy). Panels c) and d) of Figure 5 show that the decrease in dynamic stress drop for self-arresting ruptures (Models A) is larger than the one inferred for runaway ruptures (Models B). Furthermore, the increase in breakdown stress drop is smaller for self-arresting ruptures, and this results in a smaller ratio between dynamic and breakdown stress drop (i.e. 1/(1+S) in Figure 5 c - d), which is associated with larger spatial values of the S parameter (Figure 1). It is important to emphasize that in all these dynamic models, rupture propagation is associated with spatially variable stress drops (dynamic and breakdown).

Decreasing D_c for Models A yields runaway ruptures because fracture energy G_c decreases, yielding G_c values much smaller than those inferred for larger D_c values (> 0.4) or for Models B (see Supplementary Material Figure S4). This implies that within a given class of Models (i.e., for a given value of dynamic friction coefficient) the dissipated energy determines the self-arresting or runaway features of the dynamic rupture propagation of the induced earthquake. However, larger energy dissipation at the rupture front (i.e., fracture energy) is not sufficient to explain the occurrence of self-arresting ruptures as shown by the comparison between Panels b and a in Figure 5. More generally, self-arresting rupture depends on the assumed residual stress level, and fracture energy alone does not fully characterize the required conditions for self-arresting dynamic ruptures since the strength excess parameter S is also important and it should be considered as well (see Panels 5c and 5d).

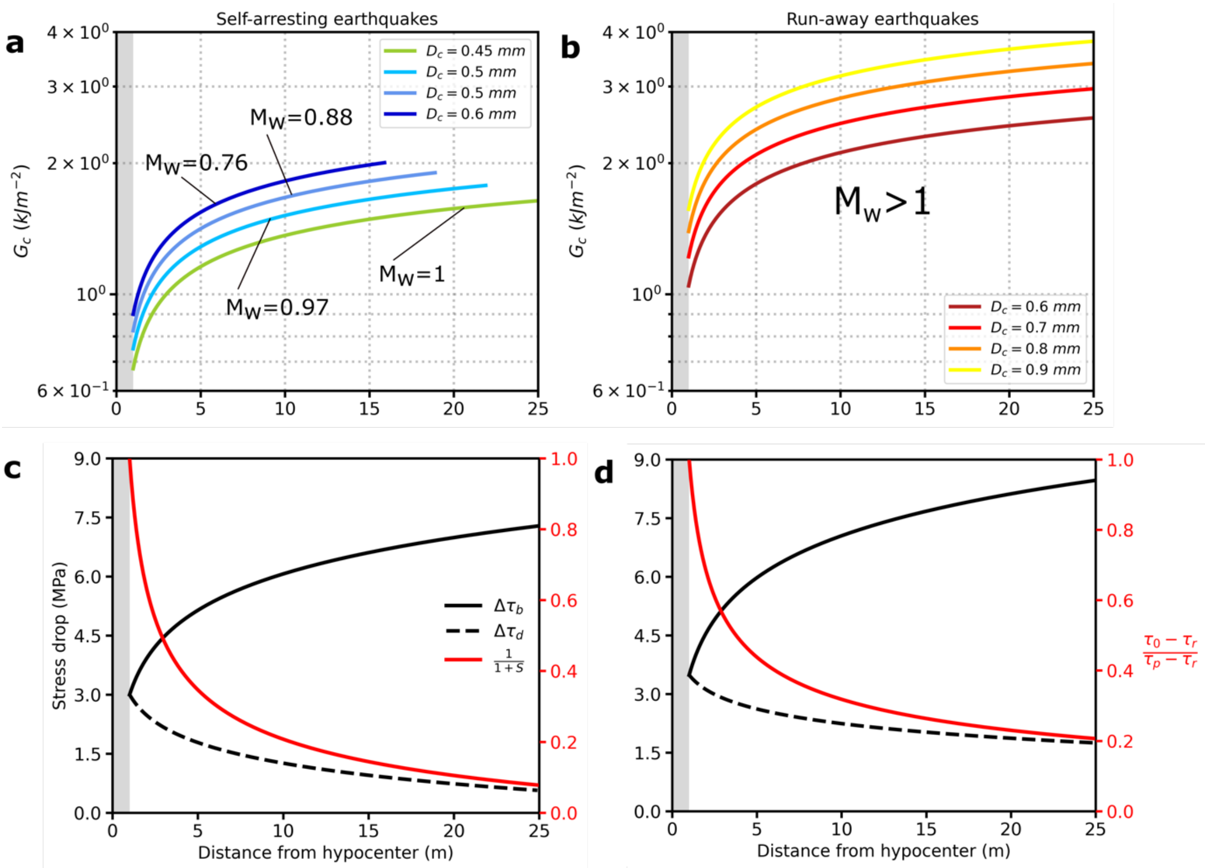

Figure 5. Fracture Energy (i.e., energy dissipation) and stress drop comparison for the two sets of Models A and B. **(a-b)** Spatial variation of fracture energy with the distance from the hypocenter (injection point) for the set of Models A and B, respectively. The curves for self-arresting models (Models A) are interrupted to indicate the arrest points of the ruptures. **(c-d)** Spatial variation of stress drops with distance from the hypocenter (injection point) for sets of Models A and B, respectively. The black dashed line represents the dynamic stress drop, the black solid line depicts the breakdown stress drop, and the red solid line illustrates the ratio between these two stress drops, labeled by the 1/(1+S) parameter to link the curve to the strength parameter S.

5.2 Dynamic load

The behavior of peak slip velocity during dynamic propagation (Figures 3 and 4) suggests that the differences between self-arresting and runaway ruptures can be interpreted in terms of the dynamic load sustaining rupture front propagation. Despite the large dissipation at the rupture front (i.e., fracture energy), the dynamic load is much larger for runaway ruptures than for self-arresting ones. A straightforward method to represent the dynamic load at the rupture front is computing the shear stress at a given point on the fault, which is a function of slip velocity. Fukuyama and Madariaga (1998) proposed the following relationship:

$$\sigma(x,t) = -\frac{G}{2\beta}\,\dot{\delta}(x,t) + \int_{\Sigma}\int_{0}^{t} K(x-\xi\,;\,t-t')\,\dot{\delta}(\xi\,,t)\,dt'\,dS \qquad (4)$$

where β is the shear wave velocity, $\dot{\delta}$ (x,t) is the slip velocity function and K is the kernel representing the dynamic interaction among those points that are slipping behind the rupture front. The integral is computed over the portion of the fault Σ that slipped at time t in which the rupture front has reached the point x on the fault. Equation (4) highlights that the contribution to shear stress at a given point is composed of two terms: an instantaneous contribution determined by the slip velocity evolution at that point in space and time (i.e., a radiation damping term), and the integral term which represents the dynamic interactions of the points on the fault behind the rupture front that are still slipping with decreasing values of slip velocity. We can therefore infer that higher slip velocity values are associated with larger dynamic load at the rupture tip. This discussion relates to the size of the cohesive zone, which is the portion of the fault composed of the points located behind the rupture tip that are undergoing dynamic weakening and are expected to have the largest values of slip velocity around the peak slip rate. Therefore, they provide the largest contributions to the dynamic interactions (the integral term in equation 4) and to the dynamic load at the rupture front.

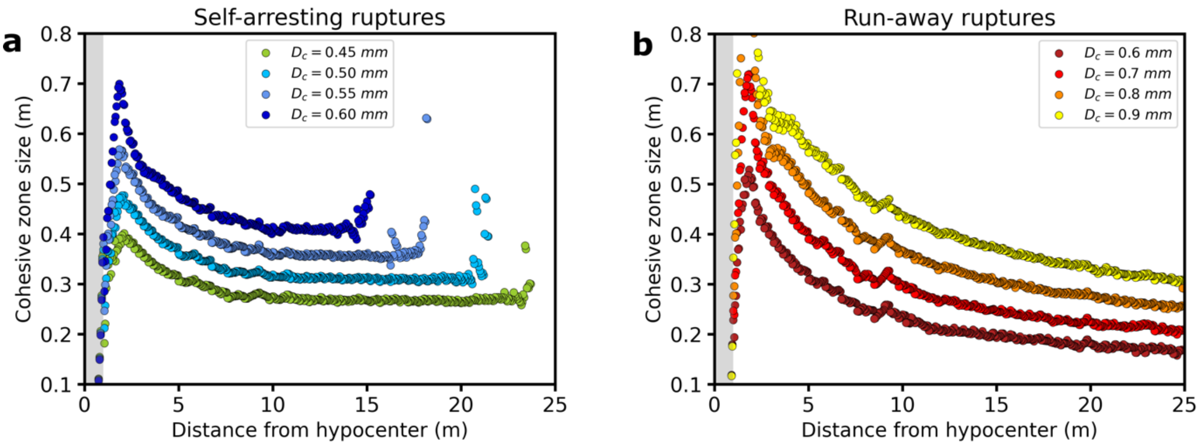

Figure 6. Cohesive zone behavior for set Models A and B. **(a-b)** The two panels respectively show the cohesive zone size with respect to the hypocentral distance (injection point), of the self-arresting (set Models A) and runaway ruptures (set Models B).

Figure 6 shows the cohesive zone sizes for self-arresting (Panel a) and runaway (Panel b) ruptures measured for the different ranges of D_c. The size of the cohesive zone is measured from the breakdown time (i.e., the time window representing the duration of dynamic weakening) of each single fault point multiplied by its local rupture speed (Day et al., 2005; Wollherr et al., 2018). Across the first 5-7.5 meters of rupture propagation away from the nucleation patch the cohesive zone shrinks for both self-arresting and runaway ruptures. This is associated with an increase of peak slip velocity and with rupture acceleration following the nucleation (Figures 3 and 4). However, for self-arresting ruptures the cohesive zone size becomes nearly constant (Figure 6a) as soon as the rupture stops accelerating (stage II in Figure 3), unlike for runaway ruptures where the cohesive zone size continuously decreases (Figure 6b and Figure S5). This key observation is associated with the decrease of peak slip velocity and rupture velocity (stages III and IV of Figure 3a and b). This corroborates that the size of the cohesive zone is linked to both slip velocity and rupture speed evolution during dynamic rupture propagation (Day et al., 2005).

We next discuss the distinctive features of self-arresting and runaway ruptures by analyzing the ratio between peak slip velocity and rupture speed. Figure 7 shows this ratio as a function of the distance from the nucleation patch. After an initial stage in which rupture speed increases more than peak slip velocity for both model classes (A and B), self-arresting ruptures are characterized by a nearly constant ratio between peak slip velocity and rupture speed, suggesting that they both decrease during the deceleration phase at the same rate in space. In contrast, in runaway ruptures peak slip velocity increases more than rupture speed because the shrinking of the cohesive zone decreases due to the reduced rupture acceleration (Figure 6b).

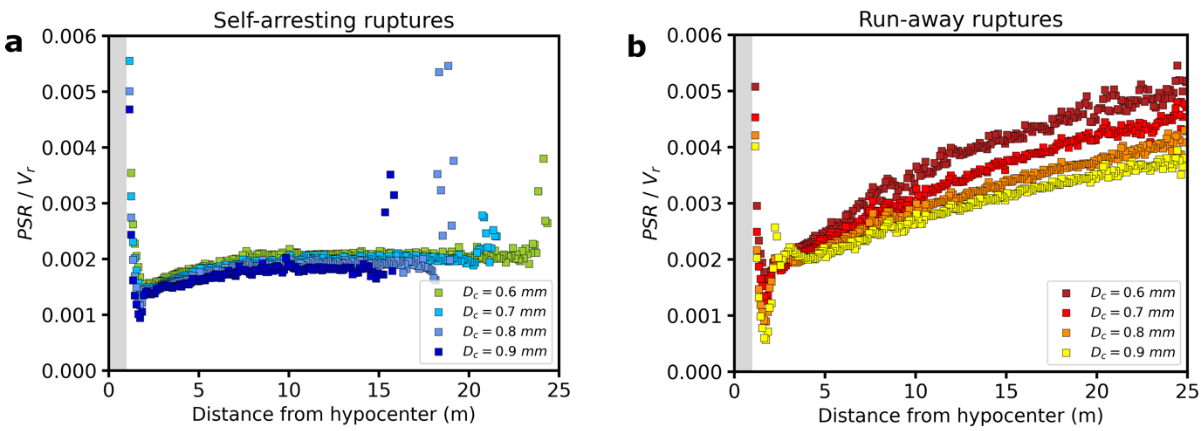

Figure 7. Peak slip rate variation normalized by the rupture speed for the set of Models A and B. **(a-b)** Showing respectively the spatial variation of the ratio between the peak slip rate of the rupture and the rupture speed with the hypocentral distance (injection point), for self-arresting (set Models A) and runaway ruptures (set Models B).

5.3 The dynamics of decelerating ruptures

The spatial gradient of strength excess, breakdown and dynamic stress drop caused by fluid injection in a pressurized patch determines interesting features for a self-arresting rupture characterized by a decelerating rupture front propagation over an extended portion of the fault. Figure 3 shows that the decelerating rupture front propagates over nearly 60% of the radius of the pressurized patch. The first key feature is the coupling between peak slip velocity and rupture velocity. This is further investigated in Figure 8 (Panels a and c) showing the slip velocity time histories and the evolution of rupture velocity in different fault positions along the strike direction for the simulations with $D_c = 0.6$ mm. Runaway ruptures are characterized by an increasing peak slip velocity and rupture speed, with a constant asymptotic residual value of slip rate, as expected for crack-like models (0.4-0.5 m/s). On the contrary, self-arresting ruptures show an initial rupture acceleration with increasing peak slip velocities, followed by a deceleration with decreasing peak slip velocity. Unlike runaway ruptures, self-arresting ruptures display a decreasing asymptotic residual value of slip rate during the deceleration stages. This does not occur during the initial acceleration stage of self-arresting rupture. Figure 8 b and d show a zoom of the slip velocity evolution during the first 5 meters from nucleation. During the initial acceleration stage slip velocity increases for both self-arresting and runaway ruptures, but the former have smaller values than the latter. Slip velocities for self-arresting ruptures remain smaller than 1 m/s, differing from runaway ruptures that exceed 1 m/s after a few meters from nucleation.

This analysis yields two main implications. First, it further corroborates that tiny differences in the residual stress due to the adopted dynamic friction coefficients and the spatial gradient of normal stress result in spatially variable dynamic stress drop and strength parameter S, determining the self-arresting features. Second, for self-arresting ruptures during the deceleration stage, the asymptotic residual slip velocity value decreases during dynamic propagation approaching zero. This implies that during rupture deceleration and arrest, a crack-like model becomes a pulse like rupture, without exhibiting any stress undershoot (Lambert et al. 2021), encountering any fault width barrier (Weng & Ampuero, 2019), or facing bi-material contrast (Ampuero & Ben-Zion, 2008).

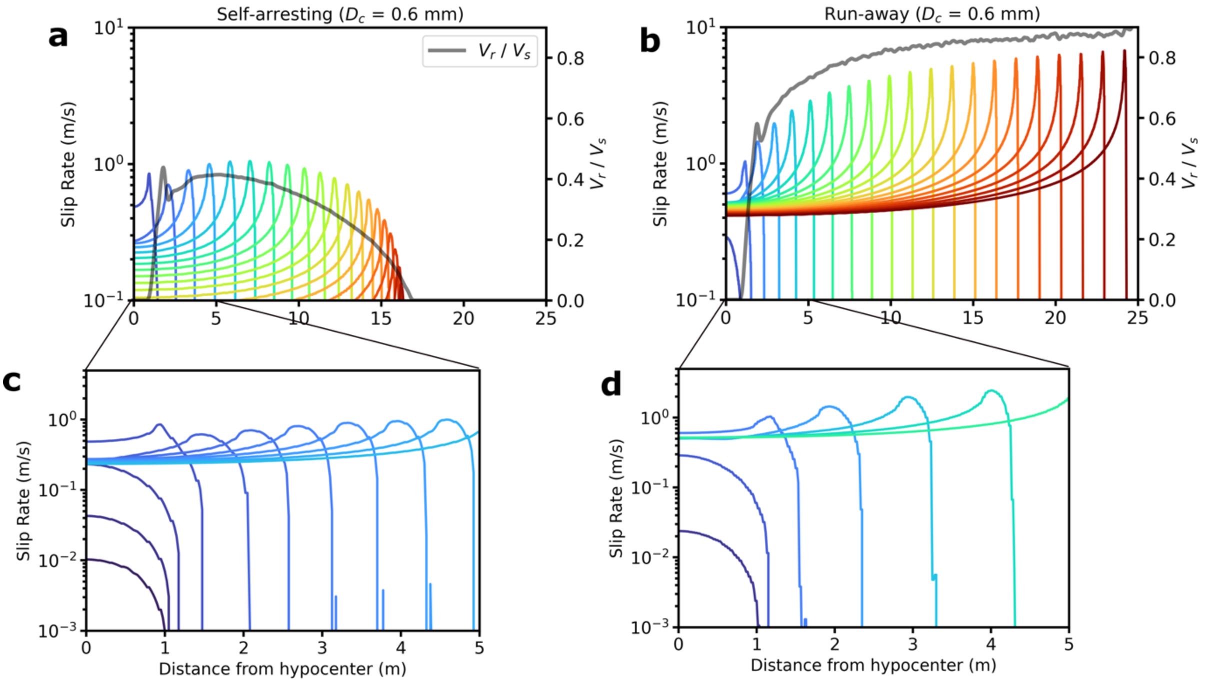

Figure 8. Evolution of slip rate and rupture speed for two example ruptures with the same D_c (0.6mm) in the sets of Models A and B. Panels **(a-c)** display the slip rate evolution at different timesteps, indicated by the colormap, and the evolution of the rupture speed depicted by the gray solid line, for self-arresting (set Models A) and run-away (set Models B) ruptures, respectively. **(b-d)** Zooming in on the initial 5 meters of the rupture extension to emphasize the evolution of the slip rate during nucleation and the initial acceleration outside the nucleation patch.

5.4 Implications for earthquake mechanics

Although the stress conditions modeled in this work are carefully selected, we believe that they are representative of fluid pressurization on a relatively homogeneous fault. While initial stress heterogeneity is a common condition to model dynamic ruptures on active faults (Ripperger et al., 2007; Ma et al. 200; Tago et al. 2012; Tinti et al., 2021; among many others), we believe that simulating dynamic propagation for a stress configuration characterized by a relatively smooth spatial gradient is of interest for studying induced seismicity. The results obtained in this work highlight distinct dynamic aspects of a decelerating rupture front that deserve to be further investigated under a wider range of initial conditions.

Notably, in our simulations the residual stress level (i.e., dynamic stress) is not constant in space and exhibits spatial gradients due to the effective normal stress changes induced by pore pressure perturbations. This is different from the conditions commonly adopted in linear elastic fracture mechanics (Galis et al., 2017; Brener and Bouchbinder, 2021; Kammer et al., 2024).

In particular, while runaway ruptures characterized by a dynamic propagation at increasing or nearly constant rupture velocity (i.e., without deceleration) are coherent with crack-like models, in which slip velocity evolves from its peak to an invariant residual value, self-arresting ruptures characterized by the propagation of a decelerating rupture front over an extended fault dimension exhibit unconventional features not completely coherent with pure crack-like models (as evidenced by the decreasing residual slip velocity values behind the decelerating rupture front). This feature represents a deviation from predictions from linear elastic fracture mechanics, and it is not usually observed in dynamic simulations with linear slip weakening law and heterogeneous prestress. It is worth noting that in our dynamic simulations we do not prescribe the Griffith energy balance at the crack tip (Freund, 1989; Galis et al., 2017; Kammer et al., 2024), for which the energy release rate (energy flow at the crack-tip) is equal to the fracture energy (i.e., the energy dissipated at the rupture front). In other words, we do not assume that the energy flow is equal to the dissipated energy at the rupture tip. Indeed, the solution of the 3D dynamic rupture propagation is obtained by assuming the constitutive law (the linear slip weakening in our case) and the collinearity between slip velocity and shear traction. This explains why self-arresting ruptures are not uniquely characterized by larger energy dissipation at the rupture tip; rather, the larger spatial decrease of dynamic stress drop (as mapped by spatial gradient of the strength parameter S) determines self-arresting features.

6. Conclusions

In this paper we have performed a series of 3D simulations to model the dynamic rupture of a pressurized patch stimulated through fluid injection within the nucleation zone. To our knowledge, these represent the first dynamic rupture simulations for an induced micro-earthquake on a decametric-scale planar fault (50 m length). Previously, only Liu and Lapusta (2008) modeled a ~2 magnitude micro-earthquake repeater of the San Andreas Fault through 3D seismic cycle simulation. The fault geometry and the pore fluid pressure changes have been modeled to reproduce the stimulation experiments envisioned by the FEAR project in the Bedretto Lab (BULGG). In particular, the pore pressure profile along the fault radius and around the injection borehole has been computed through poro-elastic simulation of the fault zone. The initial stress is kept constant to investigate the role of the spatial gradient of effective normal stress. The two classes of models simulated in this study differ in their values of the dynamic friction coefficient and in the range of their values of the critical slip weakening distance. Models B have a smaller dynamic friction coefficient ($\mu_d = 0.15$) and larger D_c values ranging from 0.60 mm to 0.90 mm. They result in runaway ruptures propagating over the entire pressurized patch, without any deceleration of the rupture front. This behavior is obtained also using smaller values of the critical slip weakening distance D_c, which have not been discussed because they yield supershear ruptures. On the contrary, Models A, characterized by a higher dynamic friction coefficient ($\mu_d = 0.21$) and smaller D_c values ranging from 0.45 mm to 0.60 mm, display self-arresting rupture within the pressurized patch. Decreasing D_c for this class of Models A would yield runaway ruptures.

The results of this study are of relevance to discuss the dynamic propagation of rupture during an induced earthquake characterized by a spatially variable, continuously increasing effective normal stress governed by the pore fluid pressurization of the fault patch. This causes spatially variable peak and residual stress values, which result in a spatially variable strength excess, breakdown and dynamic stress drops. In this configuration, decreasing the residual stress by changing the dynamic coefficient of friction makes the fault more unstable, yielding runaway ruptures for a broad range of D_c values. This results in generating smooth, spatially variable frictional strength, as described by the spatial evolution of the S parameter. While this is expected, a tiny increase of the dynamic friction coefficient, which is still representative of a weak fault ($\mu_d \approx 0.2$), can generate self-arresting ruptures characterized by a large spatial increase (gradient) of the S parameter caused by the spatial decrease in dynamic stress drop. In this configuration, we have found a range of D_c values for which self-arresting ruptures are characterized by the propagation of a decelerating rupture front over a finite portion of the pressurized patch. Self-arresting ruptures do not reach the edge of the pressurized patch, unlike runaway ruptures.

Our simulations corroborate that self-arresting and runaway ruptures are determined by the stress state within the pressurized patch. However, the analysis of the dynamics of a decelerating propagating rupture yields interesting and somehow surprising results.

We have shown that the distinction between self-arresting and runaway ruptures cannot be explained solely in terms of fracture energy (i.e., the energy dissipated at the rupture front); that is, ruptures are not self-arresting because they dissipate more energy at the tip. Runaway ruptures dissipate more energy than self-arresting ones, even if decreasing fracture energy (by decreasing D_c) transforms self-arresting ruptures into runaway ones. The spatial variation of frictional strength caused by the spatially increasing normal stress within the pressurized patch is the key feature to enable self-arresting, because it is determining the dynamic load sustaining the propagation of the rupture front. Indeed, the behavior of slip velocity, rupture speed and cohesive zone size suggests that dynamic load, supporting rupture front propagation, is larger for runaway ruptures. On the contrary, we can conclude that for self-arresting ruptures the dynamic load is not large enough to maintain the dynamic rupture propagation causing rupture deceleration associated with a nearly constant size of the cohesive zone and decreasing peak slip velocity values until the final rupture arrest. The peculiar feature of this dynamic propagation is the spatially variable dynamic stress drop and strength excess.

The dynamic propagation of an induced self-arresting rupture over a finite extension of the pressurized patch generates a slip velocity field that differs from that obtained for runaway ruptures, characterized by the propagation at constant or increasing rupture speed. The most evident feature is the decrease of peak slip velocity associated with the decelerating rupture and the nearly constant cohesive zone size. The other relevant feature is the decrease of the residual slip velocity value (asymptotic value for a crack-like rupture), which decreases during deceleration becoming nearly zero. This means that the initial crack-like rupture retrieved during the acceleration stage becomes a pulse-like rupture at the arrest.

The results of this study, obtained under specific stress conditions, are applied to a realistic scenario of an induced earthquake at BULGG. Nonetheless, they allow us to highlight how the study of the rupture dynamics of an induced earthquake involves peculiarities relevant to the mechanics of earthquakes. The spatially variable normal stress causes variations of frictional strength and spatially variable breakdown and dynamic stress drops. This might have implications for radiated energy and frequency contents of ground motions caused by induced earthquakes. Although further investigations are needed to account for prestress heterogeneity, we emphasize the importance of exploring rupture deceleration over a finite portion of a pressurized patch.

Acknowledgements

This study has received funding from the European Research Council (ERC) under the European Union’s Horizon 2020 research and innovation programme (grant agreement No 856559). MC participated in this work as Principal Investigator of the European Research Council (ERC) project FEAR (grant agreement No 856559) under the European Community’s Horizon 2020 Framework Programme. FM, LDZ, APL and ET also participated in this work in the framework of the European Research Council (ERC) project FEAR (grant agreement No 856559) under the European Community’s Horizon 2020 Framework Programme.

AAG acknowledges additional support by the European Union's Horizon 2020 research and innovation program (TEAR ERC Starting; grant no. 852992) and Horizon Europe (ChEESE-

2P, grant no. 101093038; DT-GEO, grant no. 101058129; and Geo-INQUIRE, grant no. 101058518), the National Science Foundation (grant nos. EAR-2225286, EAR-2121568, OAC-2139536, OAC-2311208), and the National Aeronautics and Space Administration (grant no. 80NSSC20K0495).
We thank Ravil Dorozhinskii, Thomas Ulrich and the SeisSol team (see www.seissol.org).
We acknowledge the CINECA award under the ISCRA initiative, for the availability of high-performance computing resources and support.

Open Research

We use the SeisSol software package available on GitHub (https://github.com/SeisSol/SeisSol) to simulate all dynamic models. We use SeisSol, version {202103_Sumatra-686-gf8e01a54} (master branch on commit dd018b3398258a23ec2a33c74bd7f31b503dcca6, v1.1.3-362-gdd018b33). The procedure to download and run the code is described in the SeisSol documentation (seissol.readthedocs.io/en/latest/). Downloading and compiling instructions are at https://seissol.readthedocs.io/en/latest/compiling-seissol.html. Instructions for setting up and running simulations are at https://seissol.readthedocs.io/en/latest/configuration.html. Quickstart containerized installations and introductory materials are provided in the docker container and Jupyter Notebooks at {https://github.com/SeisSol/Training. Example problems and model configuration files are provided at https://github.com/SeisSol/Examples, many of which reproduce the SCEC 3D Dynamic Rupture benchmark problems described at https://strike.scec.org/cvws/benchmark_descriptions.html.
All data required to reproduce the dynamic rupture scenarios are available at ... .
The data will be fully archived at Zenodo at acceptance.

References

Abercrombie, R. E. (1995). Earthquake source scaling relationships from− 1 to 5 ML using seismograms recorded at 2.5-km depth. Journal of Geophysical Research: Solid Earth.

Abercrombie, R. E. (2021). Resolution and uncertainties in estimates of earthquake stress drop and energy release. Philosophical Transactions of the Royal Society A.

Abercrombie, R. E., & Rice, J. R. (2005). Can observations of earthquake scaling constrain slip weakening?. Geophysical Journal International.

Achtziger-Zupančič, Peter & Ceccato, Alberto & Zappone, Alba & Pozzi, Giacomo & Shakas, Alexis & Amann, Florian & Behr, Whitney & Botero, Daniel & Giardini, Domenico & Hertrich, Marian & Jalali, Mohammadreza & Ma, Xiaodong & Meier, Men-Andrin & Osten, Julian & Wiemer, Stefan & Cocco, Massimo. (2024). Selection and Characterisation of the Target Fault for Fluid-Induced Activation and Earthquake Rupture Experiments. 10.5194/egusphere-2024-586.

Ampuero, J. P., & Ben-Zion, Y. (2008). Cracks, pulses and macroscopic asymmetry of dynamic rupture on a bimaterial interface with velocity-weakening friction. Geophysical Journal International, 173(2), 674-692.

Andrews, D. J. (1976). Rupture velocity of plane strain shear cracks. Journal of Geophysical Research, 81(32), 5679-5687.

Andrews, D. J. (1985). Dynamic plane-strain shear rupture with a slip-weakening friction law calculated by a boundary integral method. Bulletin of the Seismological Society of America, 75(1), 1-21.

Allmann, B. P., & Shearer, P. M. (2007). Spatial and temporal stress drop variations in small earthquakes near Parkfield, California. Journal of Geophysical Research: Solid Earth.

Allmann, B. P., & Shearer, P. M. (2009). Global variations of stress drop for moderate to large earthquakes. Journal of Geophysical Research: Solid Earth.

Bai, K., & Ampuero, J. P. (2017). Effect of seismogenic depth and background stress on physical limits of earthquake rupture across fault step overs. Journal of Geophysical Research: Solid Earth, 122(12), 10-280.

Barbot, S., Lapusta, N., & Avouac, J. P. (2012). Under the hood of the earthquake machine: Toward predictive modeling of the seismic cycle. Science, 336(6082), 707-710.

Barras, F., Thøgersen, K., Aharonov, E., & Renard, F. (2023). How do earthquakes stop? Insights from a minimal model of frictional rupture. Journal of Geophysical Research: Solid Earth, 128(8), e2022JB026070.

Biemiller, J., Gabriel, A. A., & Ulrich, T. (2023). Dueling dynamics of low-angle normal fault rupture with splay faulting and off-fault damage. Nature Communications, 14(1), 2352.

Bizzarri, A. (2010). How to promote earthquake ruptures: Different nucleation strategies in a dynamic model with slip-weakening friction. Bulletin of the Seismological Society of America, 100(3), 923-940.

Bolton, D. C., Affinito, R., Smye, K., Marone, C., & Hennings, P. (2023). Frictional and poromechanical properties of the Delaware Mountain Group: Insights into induced seismicity in the Delaware Basin. Earth and Planetary Science Letters, 623, 118436.

Brener, E. A., & Bouchbinder, E. (2021). Unconventional singularities and energy balance in frictional rupture. Nature communications, 12(1), 2585.

Bröker, K., & Ma, X. (2022). Estimating the least principal stress in a granitic rock mass: systematic mini-frac tests and elaborated pressure transient analysis. Rock Mechanics and Rock Engineering, 55(4), 1931-1954.

Bröker, K., X. Ma, N. Gholizadeh Doonechaly, A. P. Rinaldi, M. Hertrich, A. Obermann, V. Clasen Repolles, S. Wiemer, D. Giardini, H. Maurer (2023). Hydro-geomechanical observations during multistage hydraulic stimulation at the Bedretto Underground Laboratory, Switzerland. In: Proceedings of the 57th US Rock Mechanics/Geomechanics Symposium, Atlanta, Georgia, USA.

Candela, T., Wassing, B., Ter Heege, J., & Buijze, L. (2018). How earthquakes are induced. Science, 360(6389), 598-600.

Cappa, F., Scuderi, M. M., Collettini, C., Guglielmi, Y., & Avouac, J. P. (2019). Stabilization of fault slip by fluid injection in the laboratory and in situ. Science advances, 5(3), eaau4065.

Cebry, S. B. L., Ke, C. Y., & McLaskey, G. C. (2022). The Role of Background Stress State in Fluid-Induced Aseismic Slip and Dynamic Rupture on a 3-m Laboratory Fault. Journal of Geophysical Research: Solid Earth, 127(8), e2022JB024371.

Ciardo, F., & Rinaldi, A. P. (2022). Impact of injection rate ramp-up on nucleation and arrest of dynamic fault slip. Geomechanics and Geophysics for Geo-Energy and Geo-Resources, 8(1), 28.

Cocco, M., & Rice, J. R. (2002). Pore pressure and poroelasticity effects in Coulomb stress analysis of earthquake interactions. Journal of Geophysical Research: Solid Earth, 107(B2), ESE-2.

Cocco, M., Tinti, E., & Cirella, A. (2016). On the scale dependence of earthquake stress drop. Journal of Seismology.

Cornet, F. H. (2012). The relationship between seismic and aseismic motions induced by forced fluid injections. Hydrogeology journal, 20(8), 1463.

Cornet, F. H. (2016). Seismic and aseismic motions generated by fluid injections. Geomechanics for Energy and the Environment, 5, 42-54.

Das, S., & Aki, K. (1977). Fault plane with barriers: A versatile earthquake model. Journal of geophysical research, 82(36), 5658-5670.

Dalguer, L. A., & Day, S. M. (2009). Asymmetric rupture of large aspect-ratio faults at bimaterial interface in 3D. Geophysical Research Letters, 36(23).

Dal Zilio, L., Hegyi, B., Behr, W., & Gerya, T. (2022). Hydro-mechanical earthquake cycles in a poro-visco-elasto-plastic fluid-bearing fault structure. Tectonophysics, 838, 229516.

Dumbser, M., & Käser, M. (2006). An arbitrary high-order discontinuous Galerkin method for elastic waves on unstructured meshes—II. The three-dimensional isotropic case. Geophysical Journal International, 167(1), 319-336.

Ellsworth, W. L. (1995). Seismic evidence for an earthquake nucleation phase. Science.

Ellsworth, W. L. (2013). Injection-induced earthquakes. Science, 341(6142), 1225942.

Fukuyama, E., & Madariaga, R. (1998). Rupture dynamics of a planar fault in a 3D elastic medium: rate-and slip-weakening friction. Bulletin of the Seismological Society of America.

Gabriel, A. A., Ampuero, J. P., Dalguer, L. A., & Mai, P. M. (2012). The transition of dynamic rupture styles in elastic media under velocity-weakening friction. Journal of Geophysical Research: Solid Earth, 117(B9).

Gabriel, A. A., Garagash, D. I., Palgunadi, K. H., & Mai, P. M. (2023). Fault-size dependent fracture energy explains multi-scale seismicity and cascading earthquakes. arXiv preprint arXiv:2307.15201.

Gabriel, A. A., Ulrich, T., Marchandon, M., Biemiller, J., & Rekoske, J. (2023). 3D Dynamic Rupture Modeling of the 6 February 2023, Kahramanmaraş, Turkey M w 7.8 and 7.7 Earthquake Doublet Using Early Observations. The Seismic Record, 3(4), 342-356.

Galis, M., Ampuero, J. P., Mai, P. M., & Cappa, F. (2017). Induced seismicity provides insight into why earthquake ruptures stop. Science advances.

Galis, M., Ampuero, J. P., Mai, P. M., & Kristek, J. (2019). Initiation and arrest of earthquake ruptures due to elongated overstressed regions. Geophysical Journal International, 217(3), 1783-1797.

Garagash, D. I., & Germanovich, L. N. (2012). Nucleation and arrest of dynamic slip on a pressurized fault. Journal of Geophysical Research: Solid Earth, 117(B10).

Geubelle, P. H., & Kubair, D. V. (2001). Intersonic crack propagation in homogeneous media under shear-dominated loading: numerical analysis. Journal of the Mechanics and Physics of Solids, 49(3), 571-587.

Guglielmi, Y., Cappa, F., Avouac, J. P., Henry, P., & Elsworth, D. (2015). Seismicity triggered by fluid injection–induced aseismic slip. Science, 348(6240), 1224-1226.

Grigoli, F., Cesca, S., Priolo, E., Rinaldi, A. P., Clinton, J. F., Stabile, T. A., ... & Dahm, T. (2017). Current challenges in monitoring, discrimination, and management of induced seismicity related to underground industrial activities: A European perspective. Reviews of Geophysics, 55(2), 310-340.

Grigoli, F., Cesca, S., Rinaldi, A. P., Manconi, A., López-Comino, J. A., Clinton, J. F., et al. (2018). The November 2017 Mw 5.5 Pohang earthquake: A possible case of induced seismicity in South Korea. Science.

Harris, R. A. (2017). Large earthquakes and creeping faults. Reviews of Geophysics, 55(1), 169-198.

Harris, R. A., Barall, M., Aagaard, B., Ma, S., Roten, D., Olsen, K., ... & Dalguer, L. (2018). A suite of exercises for verifying dynamic earthquake rupture codes. Seismological Research Letters, 89(3), 1146-1162.

Hunfeld, L. B., Chen, J., Niemeijer, A. R., Ma, S., & Spiers, C. J. (2021). Seismic slip-pulse experiments simulate induced earthquake rupture in the Groningen gas field. Geophysical Research Letters, 48(11), e2021GL092417.

Hubbert, M., \& Rubey, W. W. (1959). Role of fluid pressure in mechanics of overthrust faulting. Geological Society of America Bulletin.

Ida, Y. (1972), Cohesive force across the tip of a longitudinal-shear crack and Griffith's specific surface energy, J. Geophys. Res., 77.

Imanishi, K., & Ellsworth, W. L. (2006). Source scaling relationships of microearthquakes at Parkfield, CA, determined using the SAFOD pilot hole seismic array. Washington DC American Geophysical Union Geophysical Monograph Series.

Jiang, J., Erickson, B. A., Lambert, V. R., Ampuero, J. P., Ando, R., Barbot, S. D., ... & van Dinther, Y. (2022). Community-driven code comparisons for three-dimensional dynamic modeling of sequences of earthquakes and aseismic slip. Journal of Geophysical Research: Solid Earth, 127(3), e2021JB023519.

Kame, N., & Yamashita, T. (1999). A new light on arresting mechanism of dynamic earthquake faulting. Geophysical research letters, 26(13), 1997-2000.

Kammer, D. S., McLaskey, G. C., Abercrombie, R. E., Ampuero, J. P., Cattania, C., Cocco, M., ... & Tinti, E. (2024). Energy dissipation in earthquakes. arXiv preprint arXiv:2403.06916.

Kanamori, H. (1981). The nature of seismicity patterns before large earth-quakes, in Earthquake Prediction—An International Review.

Kanamori, H. (2003). Earthquake prediction: An overview. International Geophysics, 81, 1205-1216.

Ke, C. Y., McLaskey, G. C., & Kammer, D. S. (2018). Rupture termination in laboratory-generated earthquakes. Geophysical Research Letters, 45(23), 12-784.

Ke, C. Y., McLaskey, G. C., & Kammer, D. S. (2022). Earthquake breakdown energy scaling despite constant fracture energy. Nature communications, 13(1), 1005.

Keranen, K. M., Savage, H. M., Abers, G. A., \& Cochran, E. S. (2013). Potentially induced earthquakes in Oklahoma, USA: Links between wastewater injection and the 2011 Mw 5.7 earthquake sequence. Geology.

Kim, K.-H., Ree, J.-H., Kim, Y., Kim, S., Kang, S. Y., \& Seo, W. (2018). Assessing whether the 2017 M w 5.4 Pohang earthquake in South Korea was an induced event. Science.

Kostrov, B. V. (1964). Self-similar problems of propagation of shear cracks. Journal of Applied Mathematics and Mechanics, 28(5), 1077-1087.

Lapusta, N., & Liu, Y. (2009). Three-dimensional boundary integral modeling of spontaneous earthquake sequences and aseismic slip. Journal of Geophysical Research: Solid Earth, 114(B9).

Larochelle, S., Lapusta, N., Ampuero, J. P., & Cappa, F. (2021). Constraining fault friction and stability with fluid-injection field experiments. Geophysical Research Letters, 48(10), e2020GL091188.

Lee, K. K., Ellsworth, W. L., Giardini, D., Townend, J., Ge, S., Shimamoto, T., ... & Langenbruch, C. (2019). Managing injection-induced seismic risks. Science, 364(6442), 730-732.

Lesko, K.: The Sanford Underground Research Facility at Homestake (SURF), Physics Procedia, 61, 542–551.

Liu, L. and Zoback, M. D.: The effect of topography on the state of stress in the crust: application to the site of the Cajon Pass Scientific Drilling Project, J. Geophys. Res.

Liu, Y., & Lapusta, N. (2008). Transition of mode II cracks from sub-Rayleigh to intersonic speeds in the presence of favorable heterogeneity. Journal of the Mechanics and Physics of Solids, 56(1), 25-50.

Lui, S. K., & Lapusta, N. (2018). Modeling high stress drops, scaling, interaction, and irregularity of repeating earthquake sequences near Parkfield. Journal of Geophysical Research: Solid Earth, 123(12), 10-854.

Ma, X., Hertrich, M., Amann, F., Bröker, K., Gholizadeh Doonechaly, N., Gischig, V., ... \& Giardini, D. (2022). Multi-disciplinary characterizations of the Bedretto Lab a new underground geoscience research facility. Solid Earth.

Ma, S., Custódio, S., Archuleta, R. J., & Liu, P. (2008). Dynamic modeling of the 2004 Mw 6.0 Parkfield, California, earthquake. Journal of Geophysical Research: Solid Earth, 113(B2).

Martínez-Garzón, P., Ben-Zion, Y., Abolfathian, N., Kwiatek, G., & Bohnhoff, M. (2016). A refined methodology for stress inversions of earthquake focal mechanisms. Journal of Geophysical Research: Solid Earth, 121(12), 8666-8687.

McGarr, A. (2014). Maximum magnitude earthquakes induced by fluid injection. Journal of Geophysical Research: solid earth, 119(2), 1008-1019.

Meier M.A. et al. “Activation of a natural granitic fault zone at the BedrettoLab” submitted to Solid Earth (EGU).

Miller, S. A., Collettini, C., Chiaraluce, L., Cocco, M., Barchi, M., & Kaus, B. J. (2004). Aftershocks driven by a high-pressure CO2 source at depth. Nature.

Moein, M. J., Langenbruch, C., Schultz, R., Grigoli, F., Ellsworth, W. L., Wang, R., ... & Shapiro, S. (2023). The physical mechanisms of induced earthquakes. Nature Reviews Earth & Environment, 4(12), 847-863.

Palgunadi, K. H., Gabriel, A. A., Ulrich, T., López‐Comino, J. Á., & Mai, P. M. (2020). Dynamic Fault Interaction during a Fluid‐Injection‐Induced Earthquake: The 2017 M w 5.5 Pohang Event. Bulletin of the Seismological Society of America, 110(5), 2328-2349.

Pelties, C., De la Puente, J., Ampuero, J. P., Brietzke, G. B., & Käser, M. (2012). Three‐dimensional dynamic rupture simulation with a high‐order discontinuous Galerkin method on unstructured tetrahedral meshes. Journal of Geophysical Research: Solid Earth, 117(B2).

Ramos, M. D., Thakur, P., Huang, Y., Harris, R. A., & Ryan, K. J. (2022). Working with dynamic earthquake rupture models: A practical guide. Seismological Society of America, 93(4), 2096-2110.

Rice, J. R. (1992). Fault stress states, pore pressure distributions, and the weakness of the San Andreas fault. In International geophysics (Vol. 51, pp. 475-503). Academic Press.

Rinaldi, A. P., & Rutqvist, J. (2019). Joint opening or hydroshearing? Analyzing a fracture zone stimulation at Fenton Hill. Geothermics, 77, 83-98.

Rinaldi, A. P., Rutqvist, J., Luu, K., Blanco-Martín, L., Hu, M., Sentís, M. L., ... & Kaestli, P. (2022). TOUGH3-FLAC3D: a modeling approach for parallel computing of fluid flow and geomechanics. Computational Geosciences, 26(6), 1563-1580.

Rubin, A. M., & Ampuero, J. P. (2005). Earthquake nucleation on (aging) rate and state faults. Journal of Geophysical Research: Solid Earth, 110(B11).

Schmedes, J., R. J. Archuleta, and D. Lavalle´e (2010), Correlation of earthquake source parameters inferred from dynamic rupture simulations,J. Geophys. Res.,115, B03304, doi:10.1029/2009JB006689

Scholz, C. H., & Cowie, P. A. (1990). Determination of total strain from faulting using slip measurements. Nature, 346(6287), 837-839.

Scholz, C. H., & Lawler, T. M. (2004). Slip tapers at the tips of faults and earthquake ruptures. Geophysical research letters, 31(21).

Shapiro, S. A., Krüger, O. S., Dinske, C., & Langenbruch, C. (2011). Magnitudes of induced earthquakes and geometric scales of fluid-stimulated rock volumes. Geophysics, 76(6), WC55-WC63.

Scuderi, M. M., & Collettini, C. (2016). The role of fluid pressure in induced vs. triggered seismicity: Insights from rock deformation experiments on carbonates. Scientific reports, 6(1), 24852.

Tago, J., Cruz-Atienza, V. M., Virieux, J., Etienne, V., & Sánchez-Sesma, F. J. (2012). A 3D hp-adaptive discontinuous Galerkin method for modeling earthquake dynamics. Journal of Geophysical Research: Solid Earth, 117(B9).

Tinti, E., Bizzarri, A., Piatanesi, A., & Cocco, M. (2004). Estimates of slip weakening distance for different dynamic rupture models. Geophysical research letters.

Tinti, E., Casarotti, E., Ulrich, T., Taufiqurrahman, T., Li, D., & Gabriel, A. A. (2021). Constraining families of dynamic models using geological, geodetic and strong ground motion data: The Mw 6.5, October 30th, 2016, Norcia earthquake, Italy. Earth and Planetary Science Letters, 576, 117237.

Tobin, H. J., Saffer, D. M., Castillo, D. A., & Hirose, T. (2022). Direct constraints on in situ stress state from deep drilling into the Nankai subduction zone, Japan. Geology, 50(11), 1229-1233.

Uenishi, K., and J. R. Rice (2003), Universal nucleation length for slip-weakening rupture instability under nonuniform fault loading, J. Geophys.Res.

Ulrich, T., Gabriel, A. A., Ampuero, J. P., & Xu, W. (2019). Dynamic viability of the 2016 Mw 7.8 Kaikōura earthquake cascade on weak crustal faults. Nature communications, 10(1), 1213.

Uphoff, C., May, D. A., & Gabriel, A. A. (2023). A discontinuous Galerkin method for sequences of earthquakes and aseismic slip on multiple faults using unstructured curvilinear grids. Geophysical Journal International, 233(1), 586-626.

Viesca, R. C., & Garagash, D. I. (2015). Ubiquitous weakening of faults due to thermal pressurization. Nature Geoscience, 8(11), 875-879.

Volpe, G., Pozzi, G., Collettini, C., Spagnuolo, E., Achtziger-Zupančič, P., Zappone, A., ... & Cocco, M. (2023). Laboratory simulation of fault reactivation by fluid injection and implications for induced seismicity at the BedrettoLab, Swiss Alps. Tectonophysics, 862, 229987.

Wang, L., Kwiatek, G., Renard, F., Guérin-Marthe, S., Rybacki, E., Bohnhoff, M., ... & Dresen, G. (2024). Fault roughness controls injection-induced seismicity. Proceedings of the National Academy of Sciences, 121(3), e2310039121.

Wollherr, S., Gabriel, A. A., & Uphoff, C. (2018). Off-fault plasticity in three-dimensional dynamic rupture simulations using a modal Discontinuous Galerkin method on unstructured meshes: implementation, verification and application. Geophysical Journal International.

Yeck, W. L., Hayes, G. P., McNamara, D. E., Rubinstein, J. L., Barnhart, W. D., Earle, P. S., \& Benz, H. M. (2017). Oklahoma experiences largest earthquake during ongoing regional wastewater injection hazard mitigation efforts. Geophysical Research Letters.

Zoback, M., Hickman, S., Ellsworth, W., & SAFOD Science Team. (2011). Scientific drilling into the San Andreas fault zone–an overview of SAFOD's first five years. Scientific Drilling, 11, 14-28.